

Aerodynamic Shape Optimization by Considering Geometrical Imperfections Using Polynomial Chaos Expansion and Evolutionary Algorithms

Athanasios G. Liatsikouras, Varvara G. Asouti, Kyriakos C. Giannakoglou and Guillaume Pierrot

Abstract Uncertainties, in the form of either non-predictable shape imperfections (manufacturing) or flow conditions which are not absolutely fixed (environmental) are involved in all aerodynamic shape optimization problems. In this paper, a workflow for performing aerodynamic shape optimization under uncertainties, by taking manufacturing uncertainties into account is proposed. The uncertainty quantification (UQ) for the objective function is carried out based on the non-intrusive Polynomial Chaos Expansion (niPCE) method which relies upon the CFD software as a black-box tool. PCE is combined with an evolutionary algorithm optimization platform. CAD-free techniques are used to control the shape and simultaneously generate shape imperfections; next to this, a morphing/smoothing tool adapts the CFD mesh to any new shape. In the cases presented in this paper, all CFD evaluations are performed in the OpenFOAM environment.

A. Liatsikouras

ESI Software Germany GmbH, Kruppstr. 90, 45145 Essen, Germany, e-mail: athanasios.liatsikouras@esi-group.com, thanasis.liatsi@gmail.com

V. Asouti, K. Giannakoglou

National Technical University of Athens (NTUA), School of Mechanical Engineering, Parallel CFD & Optimization Unit, Athens, Greece, e-mail: vasouti@mail.ntua.gr, kgianna@central.ntua.gr

G. Pierrot

ESI-Group, 99 Rue des Solets, 94513 Rungis, France, e-mail: guillaume.pierrot@esi-group.com

1 Introduction

A variety of stochastic and gradient-based optimization methods have been developed to cope with shape optimization problems in aerodynamics. Most of the relevant algorithms minimize (or maximize) an objective function (to be denoted as F) assuming that the flow conditions are fixed and/or the exact geometry can be manufactured. However, this is not the case in real-world applications where the flow conditions may vary and/or the manufactured shape may deviate from the CAD model. This led to the development of algorithms for shape optimization under uncertainties related to flow conditions and/or manufacturing imperfections. In the latter, the objective function to be optimized can be expressed as $\hat{F} = \hat{F}(\mathbf{c}, \mathbf{b}, F)$ to denote the dependency of \hat{F} on the stochastically varying environmental variables $\mathbf{c} \in \mathbb{R}^M$, the design vector $\mathbf{b} \in \mathbb{R}^N$ and the performance metric F .

Associated with any design under uncertainties is the process of Uncertainty Quantification (UQ) which quantifies the effect of the uncertain variables on the performance (F). In large-scale problems, Monte-Carlo [1, 9] methods are prohibitively expensive UQ techniques.

A viable alternative is the Polynomial Chaos Expansion (PCE) [11, 4]. There are two ways to implement the PCE. In the intrusive PCE, every uncertainty affecting the flow model is introduced in the governing equations, new PDEs are derived and numerically solved. In the non-intrusive PCE (niPCE), the evaluation software is used as a black-box to compute the objective function values for some data-sets (determined by the Gauss integration formulas) of the uncertain variables.

In this work, the niPCE method is used together with an evolutionary algorithm to create a workflow for shape optimization under uncertainties. CAD-free approaches are utilized for shape deformations and a mesh morphing/smoothing tool, namely the Rigid Motion Mesh Morpher (R3M) [5], for the adaptation of the CFD mesh to the changed boundary shapes.

It is R3M and its adaptive smoother that generate the geometrical imperfections this paper deals with. Three applications are demonstrated, in which the way of introducing geometrical imperfections is investigated. The first case deals with the optimization under geometrical imperfections of an S-bend duct, the second with a 2D manifold and the last with a two-element airfoil.

2 Design-Optimization Under Uncertainties

An Evolutionary Algorithm (EA), assisted by surrogate evaluation models or meta-models, is used for the optimization under uncertainties. In fact, this is the Metamodel-Assisted EA (MAEA) of the general purpose optimization platform EASY (Evolutionary Algorithms SYstem [3]) which can handle single- or multi-objective, constrained or unconstrained problems. EASY handles three populations, namely the μ parents, the λ offspring and the elite set and applies evolution operators in conformity with binary or real encoding of the design vector (\mathbf{b}). For each offspring, the

uncertainty of the function of interest F (such as drag, lift, losses, etc.) should be quantified. Since UQ using niPCE involves many calls to the CFD tool, a MAEA that uses low-cost surrogate evaluation models (radial basis functions networks) is the right method to reduce the computational cost. Local metamodels are on-line trained for each and every new individual generated during the evolution. For all but the first generations, metamodels are used to pre-evaluate the offspring population by, practically, interpolating the objective function values of some of the previously evaluated individuals and indicate the most promising members to undergo CFD-based evaluation [8].

The overall optimization workflow is presented in fig. 1. Topics such as the UQ using the niPCE, shape parameterization and mesh morphing are discussed below in more detail.

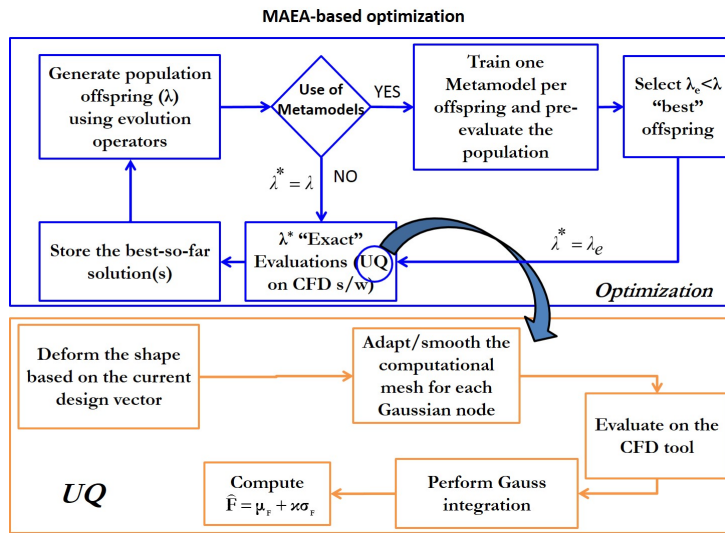


Fig. 1: Workflow for CFD-based shape optimization under uncertainties in case of geometrical imperfections. The background optimization tool is a (μ, λ) EA, with μ parents and λ offspring in each generation.

2.1 UQ using Non-Intrusive PCE

Let $F(\xi)$ be a function where ξ is a stochastic variable and $w(\xi)$ its probability density function (normal distribution). According to the PCE theory [11], F can be expressed as a linear combination of a finite subset of orthogonal polynomials $\Psi_i(\xi)$ (of degree i ; normalized Hermite polynomials)

$$F(\xi) = \sum_{i=0}^q \alpha_i \Psi_i(\xi) \quad (1)$$

with q being the chaos order. The first two statistical moments of F , i.e. its mean value and variance, can be written as

$$\mu_F = \int F(\xi) w(\xi) d\xi = \alpha_0, \quad \sigma_F^2 = \int (F(\xi) - \mu_F)^2 w(\xi) d\xi = \sqrt{\sum_{i=1}^q \alpha_i^2} \quad (2)$$

The PCE coefficients ($\alpha_i, i \in [0, q]$) result from the following integrations

$$\alpha_i = \int_{-\infty}^{\infty} F(\xi) \Psi_i(\xi) w(\xi) d\xi \quad (3)$$

computed using Gauss Quadrature (GQ). To do so, the evaluation of the problem specific function is needed at a predefined number of the so-called Gaussian nodes.

After computing the statistical moments of F through a number of evaluations of the Gaussian nodes, the appropriate objective function(s) to be maximized or minimized can be computed. Either a multi-objective optimization problem, by seeking the Pareto front on the (μ_F, σ_F) plane, or a single-objective one, by concatenating the statistical moments into a single function, can be used. In this work, the objective function (\hat{F}) to be minimized is defined as

$$\hat{F} = \mu_F + \kappa \sigma_F \quad (4)$$

where κ is a user-defined (possibly signed) weight.

2.2 Shape Parameterization and Mesh Morphing

In this paper, without loss in generality, shape parameterization is based either on Radial Basis Functions (RBFs) or cages associated with a coarse mesh that control the CFD one through properly computed Harmonic Coordinates (HC) at the nodes of the latter. The coordinates of either the RBF centers or the HC cage knots constitute the design vector $\mathbf{b} \in \mathbb{R}^N$.

Radial Basis Function Model

K RBF centers are initially selected; these can either be a subset of the surface nodes or any set of points around the shape. In the applications shown in this paper, the RBF centers are user-defined, without necessarily coinciding with surface nodes. The displacement $\Delta \mathbf{r}$ of any surface node, initially being at position \mathbf{r} , is given by

$$\Delta \mathbf{r} = \sum_{i=1}^K \mathbf{w}_i \phi(\|\mathbf{r}_{c,i} - \mathbf{r}\|) \quad (5)$$

where $\mathbf{r}_{c,i}$ is the initial position vector of the i -th RBF center, ϕ is the RBF activation function and \mathbf{w}_i are as many weights as the RBF centers, for each Cartesian direction. To compute the weights, eq. 5 is applied at the K RBF centers (separately for each Cartesian coordinate) and the resulting linear systems are numerically solved.

The HC Two-Cage Model

Harmonic coordinates (HC), initially proposed for character articulation [6], use a topologically flexible structure called “cage” to control deformations of 2D or 3D domains. An HC-based technique that may control both shape deformations and adapt the CFD mesh to the new geometry has been proposed in [7] by adopting a two-cage control mechanism. The two-cage model enables the smooth adaptation of the CFD mesh by avoiding mesh quality degradation due to large displacements at the boundaries. The cages are filled with a very coarse unstructured mesh and, by applying appropriate conditions and solving as many Laplace equations as the number of the (internal) cage control knots, the nodal HC values are computed. The HC are interpolated from the cage coarse mesh to the CFD mesh and then any CFD mesh deformation can be explicitly defined by the cage control knots displacements.

Rigid Motion Mesh Morpher

Though the RBF networks or the HC control cages could also undertake the adaptation of the CFD mesh to the updated geometry, the CFD mesh adaptation is herein controlled by a separate mesh morpher and adaptive smoother (R3M: Rigid Motion Mesh Morpher [5]). The reason is that the aforesaid smoother can also be used to generate shape variations corresponding to manufacturing imperfections. The R3M morpher is capable of displacing the internal mesh nodes by minimizing a given distortion metric by favoring rigidity in the critical directions of imminent distortion, being thus able to handle mesh anisotropies.

The computational mesh, including boundary nodes, is split into a number of overlapping stencils to be kept as rigid as possible. Let $\mathbf{u}_{i,s}$ be the ideal displacement of node i belonging to stencil s ; this stands for the displacement of the node assuming a rigid motion of the stencil it belongs to (translation and rotation, without any change in shape and size). Within the optimization loop, such an ideal situation is not possible since the displacements of the boundary nodes are determined by the value-set of design variables controlled by the EA which do not necessarily conform with the desired rigidity. To use R3M only for adapting the CFD mesh to the new boundary which is not affected by uncertainties, it suffices to minimize

$$E_1 = \sum_s w_s \sum_{i \in s} \mu_{is} (\mathbf{u}_i - \mathbf{u}_{is})^2 \quad (6)$$

where \mathbf{u}_i is the displacement of each CFD mesh node, w_s is a weight determining the importance of each stencil and μ_{is} a weight associated with node i of stencil s , μ_{is} accounts for mesh anisotropy, by favoring rigidity in directions of imminent distortion. If N_n is the number of the CFD mesh nodes, eq. 6 has $3N_n$ unknowns and E_1 can be minimized in the least squares sense.

Over and above to mesh morphing, the same tool (R3M) can additionally be used to smooth the boundary. To do so, all boundary nodes belonging to patches controlled by the optimization algorithm are considered as “handles”. The position of these handles determines the shape of the boundary based on “spring theory”. In fact, each handle is connected with its underlying node with an ideal spring, the stiffness of which is controlled by a scalar coefficient $\tilde{\lambda}$. High $\tilde{\lambda}$ values cause smaller variations in the wall shape, compared to the deterministic geometry, fig. 2. The final positions of boundary and internal mesh nodes are, then, computed by minimizing

$$E = E_1 + \tilde{\lambda} \sum_{j \in \mathbb{H}} (\mathbf{u}_j - \mathbf{V}_j^t)^2 \quad (7)$$

where \mathbf{V}_j^t are the displacements corresponding to the deterministic geometry and \mathbb{H} the set of handles.

For the needs of this paper, the smoother (last term on the r.h.s. of eq. 7) is used to create the stochastic variations in the boundary shape, by making the assumption that the uncertainty in the $\tilde{\lambda}$ value determines shape imperfections. Thus, for the known \mathbf{V}_j^t field (deterministic geometry resulting all from the EA-based search) the minimization of E (eq. 7) provides a new CFD mesh with boundary different from the deterministic one, which is affected by the stochastically varying $\tilde{\lambda}$.

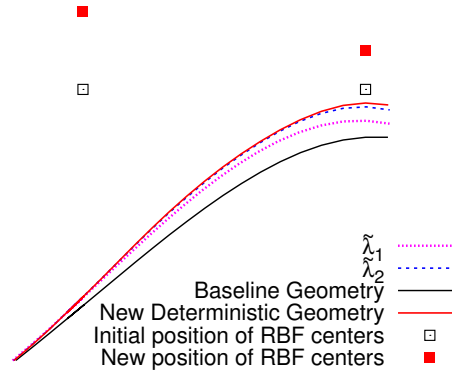


Fig. 2: Example of the effect of $\tilde{\lambda}$ coefficient in mesh deformation (2D). For the displacements computed from the RBF model (red continuous line), the minimization of E (eq. 7) determines the final nodal displacements (by considering imperfections) depending on the $\tilde{\lambda}$ values (blue/pink dashed lines for high/low values, respectively).

3 Applications

The workflow (fig. 1) for the design/optimization under uncertainties is applied to three shape optimization problems.

3.1 Optimization of an S-bend Duct

This case deals with the shape optimization of an S-bend duct by considering geometrical imperfections. The optimization aims at minimizing \hat{F} , given by eq. 4, where F stands for the total pressure losses between the duct inlet and outlet,

$$F = \frac{\int (p + \frac{1}{2}\rho\mathbf{u}^2)\mathbf{u} \cdot \mathbf{n}dS}{\int \mathbf{u} \cdot \mathbf{n}dS} \quad (8)$$

by deforming only the central curved part of the duct which is marked in red (fig. 3). In eq. 8, \mathbf{u} is the velocity vector, p is the pressure and \mathbf{n} is the outward unit normal vector at the boundaries of the flow domain.

The baseline 3D CFD mesh has been generated using CFD-GEOM [2] and consists of hexahedra close to the walls, a zone of prisms and tetrahedra everywhere else. The flow is laminar with the flow Reynolds number being equal to $Re=550$. Uncertainty in $\tilde{\lambda}$ resulting in shape variations is assumed. In specific, $\tilde{\lambda}$ follows a normal distribution with mean value $\mu_{\tilde{\lambda}}=0.017$ and standard deviation $\sigma_{\tilde{\lambda}}=0.005$.

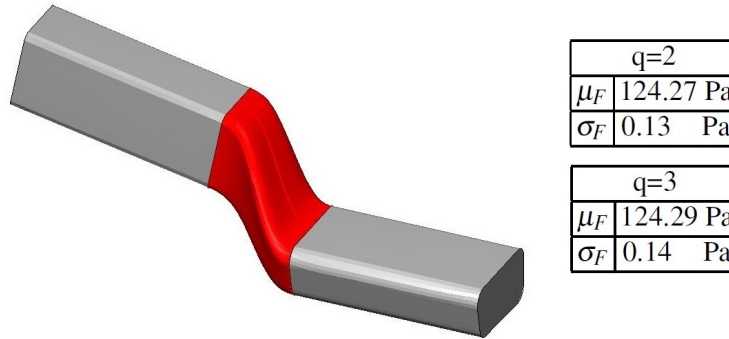


Fig. 3: S-bend duct. Left: Baseline geometry. Grey parts are kept fixed whereas the boundary marked in red is free to deform. Right: Computed mean value and standard deviation of total pressure losses (F) computed with the niPCE method for chaos order $q=2$ and 3.

For each candidate solution generated during the optimization, UQ should be performed in order to obtain the mean value and standard deviation of F . The central

curved part of the duct, which is free to deform, is controlled using an RBF model with $K=24$ RBF centers. The coordinates of the latter (as in eq. 5) are selected as design variables for the optimization workflow using EASY. An (8, 12) MAEA, with $\mu=8$ parents and $\lambda=12$ offspring, was used for the optimization; the termination criterion was set to 200 UQs. Metamodels were activated after the first 25 of them.

The optimization was performed with chaos order equal to 2. This was a reasonable selection since, as shown in fig. 3, the UQ using either $q=2$ or $q=3$ yields quite similar results; thus, $q=2$, at the cost of 3 CFD runs per UQ, was selected. The optimized geometry yields an objective function (\hat{F}) value 9.6% lower than that of the baseline. The effect of the $\tilde{\lambda}$ value in the optimized S-bend geometry for chaos order $q=2$ is shown in fig. 4.

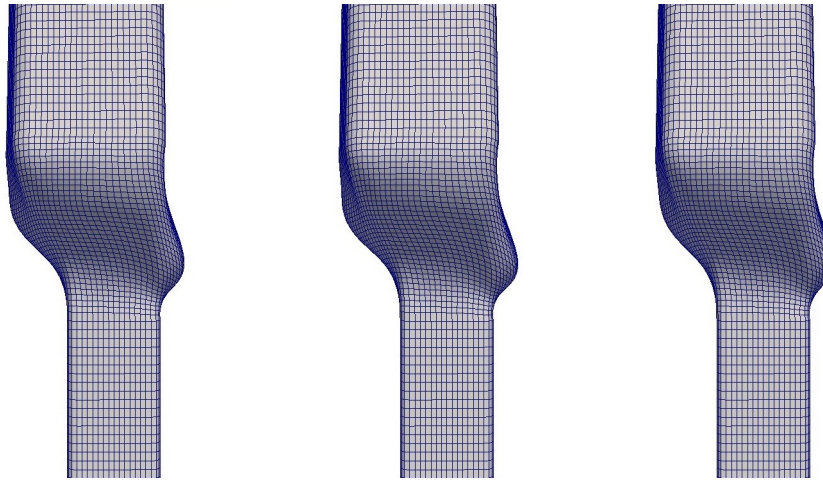


Fig. 4: S-bend duct. Effect of $\tilde{\lambda}$ to the optimized S-bend geometry for the three Gaussian nodes used for UQ with chaos order $q=2$. Differences in the volume of the second and third geometry w.r.t. the first, caused by the variation in $\tilde{\lambda}$, are 0.22% and 0.47% respectively.

It is also worth comparing the results of the optimization of the S-bend duct under geometrical uncertainties with those resulting from a run without uncertainties. For this reason, the optimization without uncertainties has been performed, followed by the UQ on the optimized geometry for $q=2$ and 3. Fig. 5 presents the convergence histories of the optimizations with and without uncertainties. In table 1, the mean value and the standard deviation of F computed for the optimized geometry are tabulated. The optimized geometry yields an objective function \hat{F} value which is by 10.4% lower than the baseline. All results have been normalized with the total pressure losses of the baseline geometry ($F_{ref}=137.84 Pa$).

Comparing tables in fig. 3 (optimization under uncertainties) and table 1 (UQ in the optimized geometry without uncertainties), some differences can be noticed.

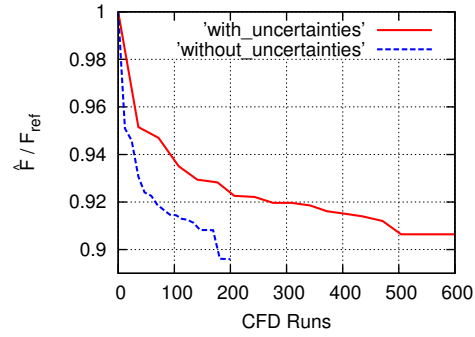


Fig. 5: S-bend duct. Convergence histories of the optimization with and without uncertainties.

Quantity	q=2	q=3
μ_F / F_{ref}	0.8961	0.8960
σ_F / F_{ref}	0.0024	0.0025

Table 1: S-bend duct. Mean value and standard deviation of total pressure losses computed with the nPCE method for $q=2$ and $q=3$ for the optimized geometry obtained from the run without considering uncertainties.

The mean value of F in latter run is lower than this resulting from the former one whereas the standard deviation of F is three times higher. In fig. 6, the total pressure field in the optimized geometries is presented. In the geometry generated by the optimization with uncertainties, the groove on the one side of the duct is smaller, which is probably the main reason for which this shape has lower standard deviation than the one generated from the optimization without uncertainties.

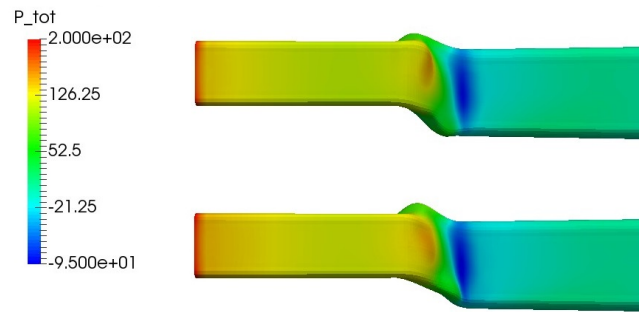


Fig. 6: S-bend duct case. Total pressure field in the optimized geometry resulted from the optimization with (top) and without (bottom) considering uncertainties.

3.2 Optimization of a 2D Manifold

The second problem deals with the shape optimization of a 2D manifold with one inlet and three outlets, for minimum $\hat{F} = \mu_F + \sigma_F$, F being the total pressure losses across the duct (as in eq. 8).

The baseline CFD mesh has approximately 140K nodes and 70K elements. An inlet velocity of $U_{in} = 0.3 m/s$ leads to a laminar flow at $Re = 1300$. A single uncertainty in the coefficient $\tilde{\lambda}$ of the morpher is assumed, causing uncertainties in the manifold shape. It is assumed that $\tilde{\lambda}$ follows a normal distribution with mean value $\mu_{\tilde{\lambda}} = 0.3$ and standard deviation $\sigma_{\tilde{\lambda}} = 0.13$.

The baseline manifold shape, extruded in the third dimension for demonstration purposes, is shown in fig. 7. Areas marked in red are free to deform. The velocity field in this geometry can be seen in fig. 8 (left).

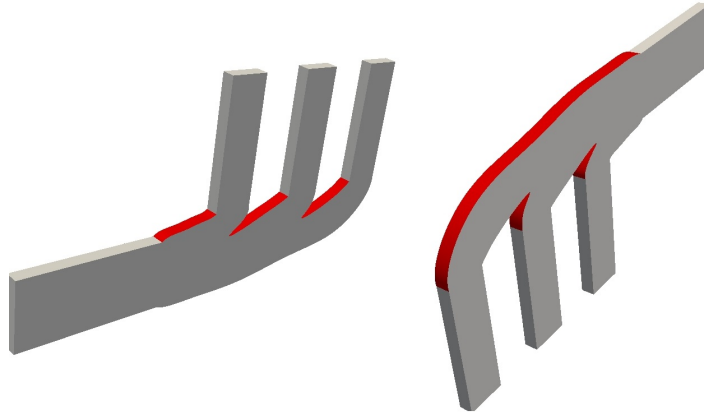


Fig. 7: Manifold case. Baseline geometry plotted in 3D for demonstration purposes. Deformable boundaries are marked in red.

The manifold is parameterized using an HC control cage with 45 knots; 28 knots out of them are allowed to vary in both directions summing up to 56 design variables in total (fig. 8; right). A (8, 12) MAEA was used and the metamodels were activated after the first 30 uncertainty quantifications. In the subsequent generations, all individuals were pre-evaluated on the metamodels and the top two of them in each generation were selected for CFD re-evaluations. After 300 UQs, a reduction in \hat{F} by $\sim 4\%$ was achieved.

The effect of chaos order on the optimization of the manifold duct is provided in table 2. Chaos order equal to 2 appears to be a good compromise in terms of accuracy and computational cost. With a single uncertain variable, namely the $\tilde{\lambda}$ coefficient of the morpher and $q=2$, three CFD evaluations per UQ are needed. The effect of the $\tilde{\lambda}$ value in the optimized geometry of the manifold is presented in fig. 10 and the convergence history in fig. 9. All results are normalized with the total

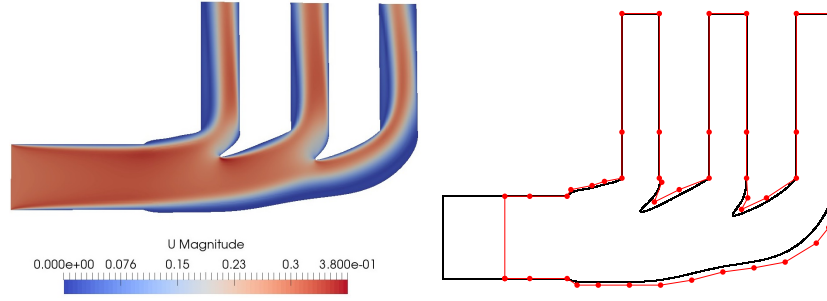


Fig. 8: Manifold case. Left: Velocity field in the baseline geometry; recirculation areas near the boundaries are the main reason for total pressure losses. Right: Baseline geometry (marked in black) and HC cage marked in red. Design variables correspond to the coordinates of the red nodes.

pressure losses of the baseline geometry. Though only a small part of the manifold was free to deform, an important reduction of the \hat{F} was achieved.

Quantity	q=2	q=3
μ_F / F_{ref}	0.9673	0.9674
σ_F / F_{ref}	8.89 E-04	8.87 E-04

Table 2: Manifold case. Mean value and standard deviation of F for $q=2$ and 3 for the optimized geometry.

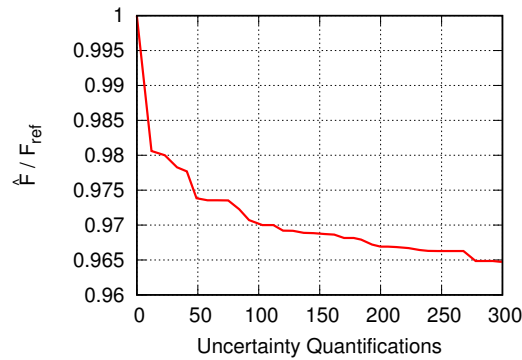


Fig. 9: Manifold case. Convergence history of the optimization under uncertainties for $q=2$. A reduction in \hat{F} of approximately 4% was achieved.

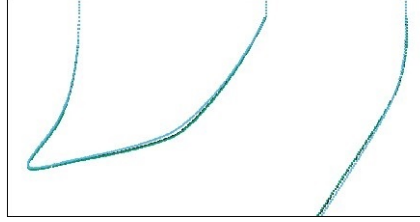


Fig. 10: Manifold case. Effect of the $\tilde{\lambda}$ value to the manifold for the three Gaussian nodes used for the UQ with $q=2$. Close-up view at the deformable and the difference between the three geometries can be observed.

3.3 Optimization of the Flap of a Two-Element Airfoil

The last case deals with the shape optimization of the flap of a two-element airfoil (fig. 11, left), without changing the shape of the main body for maximum $\hat{F} = \mu_F - \sigma_F$. The performance metric F used herein is the lift coefficient C_L . The baseline CFD mesh consists of approximately 90K nodes and 155K elements. The flow is incompressible and turbulent with freestream Mach number $M_\infty = 0.147$, Reynolds number based on the chord $Re_c = 4.23 \cdot 10^6$ and zero freestream flow angle. The Spalart–Allmaras turbulence model [10] is used. In this case, three uncertain variables, that all follow normal distributions, were assumed. Uncertain variables are the $\tilde{\lambda}$ coefficient of the morpher and the flap positioning (Δx , Δy) w.r.t. the airfoil main body. The mean value and standard deviation of the uncertain variables are tabulated in table 3.

Uncertain Variable	μ	σ
$\tilde{\lambda}$	0.10	0.03
$\Delta x / chord_{flap}$	0.0067	0.0033
$\Delta y / chord_{flap}$	-0.0033	0.0023

Table 3: Two-element airfoil. Mean values and standard deviations of the uncertain variables. Normal distribution for all of them is assumed.

The outcome of the UQ for $q=2$ is demonstrated in fig. 11 along with the main body of the airfoil, which is kept fixed, and the baseline geometry of the flap. The UQ with three variables and $q=2$ requires 27 CFD runs to compute the mean value and standard deviation of the lift coefficient.

The flap is parameterized using HC cages. The control cage consists of 17 knots summing up to 34 design variables. The main body of the airfoil is kept fixed whereas the flap is allowed to deform. For the flap, the leading and trailing edges are not allowed to move. An increase in \hat{F} by $\sim 2\%$ was achieved leading to $\mu_F = 2.6001$ and $\sigma_F = 9.27 \cdot 10^{-3}$.

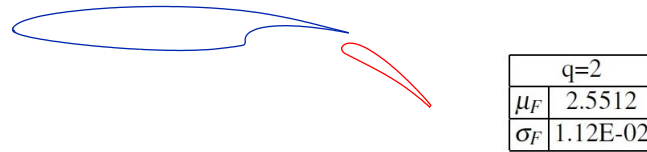


Fig. 11: Two–element airfoil. Left: Baseline geometry of the main body and flap. During the optimization, only the flap is allowed to deform whereas the main body is kept fixed. Right: Mean value and standard deviation of F for $q=2$. The lift coefficient for the baseline geometry without considering uncertainties is $C_L=2.5465$.

It can be noticed that the mean value of the lift coefficient of the optimized geometry is higher than that of in the baseline geometry whereas the standard deviation is lower. Thus, the optimized geometry operates more efficiently in a range of operating points. In fig. 12, the Mach number in the baseline and the optimized shape is demonstrated. It can be observed that, in the optimized geometry, the Mach number along the suction side is higher which is the reason of the increased lift coefficient.

The importance of using the low–cost surrogate models that EASY implements, is crucial in this case since for each candidate solution the UQ requires 27 CFD runs.

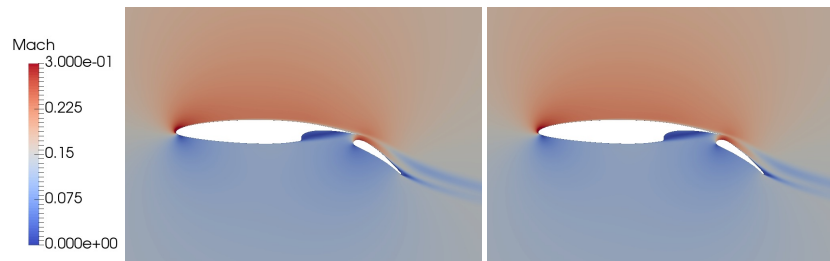


Fig. 12: Two–element airfoil. Mach number contours around the baseline (left) and the optimized (right) flap geometry. (The optimized geometry has been evaluated for the mean value of all uncertain variables.)

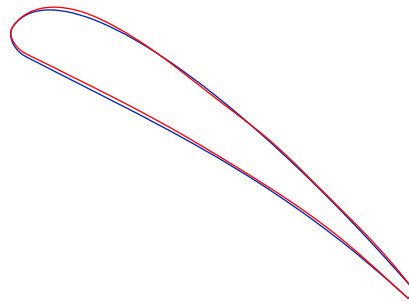


Fig. 13: Two–element airfoil. Close-up view on the flap (baseline in blue; optimized in red). The curvature of the mean camber line is increasing, to maximize the lift coefficient.

4 Closure

This paper presented a way to implement geometrical (manufacturing) imperfections during the aerodynamic shape optimization under uncertainties. This is done through the Rigid Motion Mesh Morpher (R3M) and its adaptive smoother. Uncertainty quantification was based on the non-intrusive PCE and the optimization was carried out by a metamodel–assisted EA. The use of metamodels was beneficial since it led to a reduced number of flow solutions which, in the case of UQ (with several uncertain variables), involves several calls to the CFD s/w. All these tools have been put in the form of an automated workflow for performing optimization under manufacturing uncertainties. Three applications in internal and external aerodynamics have been presented, with up to three uncertain variables related to the shapes themselves. The proposed workflow can also be used to handle operational uncertainties.

Acknowledgements The first author acknowledges the support from the People Programme (ITN Marie Curie Actions) of the European Union’s H2020 Framework Programme (MSCA-ITN-2014-ETN) under REA Grant Agreement no. 642959 (IODA project). The first author is an IODA Early Stage Researcher and PhD student at NTUA.

References

1. Asmussen S., Glyn P. (2007) Stochastic Simulation: Algorithms and Analysis, Stochastic Modelling and Applied Probability Springer New York.
2. CFD Research Corporation, CFD-ACE Theory Manual. <https://books.google.de/books?id=FinRGwAACAAJ>
3. The EASY (Evolutionary Algorithms SYstem) software. <http://velos0.ltt.mech.ntua.gr/EASY>

4. Eldred M.S., Burkardt J. (2009) Comparison of Non-Intrusive Polynomial Chaos and Stochastic Collocation Methods for Uncertainty Quantification. 47th AIAA Aerospace Sciences Meeting including The New Horizons Forum and Aerospace Exposition.
5. Eleftheriou G.S., Pierrot, G. (2014) Rigid Motion Mesh Morpher: A Novel Approach for Mesh Deformation. In: OPT-i, International Conference on Engineering and Applied Sciences Optimization, Kos Island, Greece.
6. Joshi P., Meyer M., DeRose T., Green B., Sanocki T. (2007) Harmonic Coordinates for Character Articulation. ACM Trans. Graph. 26(3), Art. No. 71.
7. Kapsoulis D.H., Tsiakas K.T., Asouti V.G., Giannakoglou, K.C. (2016) The use of Kernel PCA in Evolutionary Optimization for Computationally Demanding Engineering Applications. 2016 IEEE Symposium Series on Computational Intelligence (IEEE SSCI 2016), Athens, Greece.
8. Karakasis M.K., Giannakoglou K.C. (2006) On the use of metamodel-assisted, multi-objective evolutionary algorithms. Engineering Optimization 38(8):941-957
9. Morokoff W., Caflisch R. (1995) Quasi-Monte Carlo integration. Journal of Computational Physics 122(2):218-230
10. Spalart P.R. and Allmaras S.R. (1994) A one-equation turbulence model for aerodynamic flows. La Recherche Aérospatiale, 1:5-21.
11. Xiu D., Karniadakis G. (2002) The Wiener - Askey polynomial chaos for stochastic differential equations. SIAM Journal on Scientific Computing 24(2):619-644